PHYSICAL REVIEW C **90**, 064904 (2014)

Dielectron azimuthal anisotropy at mid-rapidity in Au + Au collisions at $\sqrt{s_{NN}} = 200$ GeV

L. Adamczyk,[1] J. K. Adkins,[23] G. Agakishiev,[21] M. M. Aggarwal,[35] Z. Ahammed,[53] I. Alekseev,[19] J. Alford,[22] C. D. Anson,[32] A. Aparin,[21] D. Arkhipkin,[4] E. C. Aschenauer,[4] G. S. Averichev,[21] A. Banerjee,[53] D. R. Beavis,[4] R. Bellwied,[49] A. Bhasin,[20] A. K. Bhati,[35] P. Bhattarai,[48] H. Bichsel,[55] J. Bielcik,[13] J. Bielcikova,[14] L. C. Bland,[4] I. G. Bordyuzhin,[19] W. Borowski,[45] J. Bouchet,[22] A. V. Brandin,[30] S. G. Brovko,[6] S. Bültmann,[33] I. Bunzarov,[21] T. P. Burton,[4] J. Butterworth,[41] H. Caines,[57] M. Calderón de la Barca Sánchez,[6] D. Cebra,[6] R. Cendejas,[36] M. C. Cervantes,[47] P. Chaloupka,[13] Z. Chang,[47] S. Chattopadhyay,[53] H. F. Chen,[42] J. H. Chen,[44] L. Chen,[9] J. Cheng,[50] M. Cherney,[12] A. Chikanian,[57] W. Christie,[4] J. Chwastowski,[11] M. J. M. Codrington,[48] G. Contin,[26] J. G. Cramer,[55] H. J. Crawford,[5] X. Cui,[42] S. Das,[16] A. Davila Leyva,[48] L. C. De Silva,[12] R. R. Debbe,[4] T. G. Dedovich,[21] J. Deng,[43] A. A. Derevschikov,[37] R. Derradi de Souza,[8] S. Dhamija,[18] B. di Ruzza,[4] L. Didenko,[4] C. Dilks,[36] F. Ding,[6] P. Djawotho,[47] X. Dong,[26] J. L. Drachenberg,[52] J. E. Draper,[6] C. M. Du,[25] L. E. Dunkelberger,[7] J. C. Dunlop,[4] L. G. Efimov,[21] J. Engelage,[5] K. S. Engle,[51] G. Eppley,[41] L. Eun,[26] O. Evdokimov,[10] O. Eyser,[4] R. Fatemi,[23] S. Fazio,[4] J. Fedorisin,[21] P. Filip,[21] E. Finch,[57] Y. Fisyak,[4] C. E. Flores,[6] C. A. Gagliardi,[47] D. R. Gangadharan,[32] D. Garand,[38] F. Geurts,[41] A. Gibson,[52] M. Girard,[54] S. Gliske,[2] L. Greiner,[26] D. Grosnick,[52] D. S. Gunarathne,[46] Y. Guo,[42] A. Gupta,[20] S. Gupta,[20] W. Guryn,[4] B. Haag,[6] A. Hamed,[47] L-X. Han,[44] R. Haque,[31] J. W. Harris,[57] S. Heppelmann,[36] A. Hirsch,[38] G. W. Hoffmann,[48] D. J. Hofman,[10] S. Horvat,[57] B. Huang,[4] H. Z. Huang,[7] X. Huang,[50] P. Huck,[9] T. J. Humanic,[32] G. Igo,[7] W. W. Jacobs,[18] H. Jang,[24] E. G. Judd,[5] S. Kabana,[45] D. Kalinkin,[19] K. Kang,[50] K. Kauder,[10] H. W. Ke,[4] D. Keane,[22] A. Kechechyan,[21] A. Kesich,[6] Z. H. Khan,[10] D. P. Kikola,[54] I. Kisel,[15] A. Kisiel,[54] D. D. Koetke,[52] T. Kollegger,[15] J. Konzer,[38] I. Koralt,[33] L. Kotchenda,[30] A. F. Kraishan,[46] P. Kravtsov,[30] K. Krueger,[2] I. Kulakov,[15] L. Kumar,[31] R. A. Kycia,[11] M. A. C. Lamont,[4] J. M. Landgraf,[4] K. D. Landry,[7] J. Lauret,[4] A. Lebedev,[4] R. Lednicky,[21] J. H. Lee,[4] M. J. LeVine,[4] C. Li,[42] W. Li,[44] X. Li,[38] X. Li,[46] Y. Li,[50] Z. M. Li,[9] M. A. Lisa,[32] F. Liu,[9] T. Ljubicic,[4] W. J. Llope,[41] M. Lomnitz,[22] R. S. Longacre,[4] X. Luo,[9] G. L. Ma,[44] Y. G. Ma,[44] D. M. M. D. Madagodagettige Don,[12] D. P. Mahapatra,[16] R. Majka,[57] S. Margetis,[22] C. Markert,[48] H. Masui,[26] H. S. Matis,[26] D. McDonald,[49] T. S. McShane,[12] N. G. Minaev,[37] S. Mioduszewski,[47] B. Mohanty,[31] M. M. Mondal,[47] D. A. Morozov,[37] M. K. Mustafa,[26] B. K. Nandi,[17] Md. Nasim,[31] T. K. Nayak,[53] J. M. Nelson,[3] G. Nigmatkulov,[30] L. V. Nogach,[37] S. Y. Noh,[24] J. Novak,[29] S. B. Nurushev,[37] G. Odyniec,[26] A. Ogawa,[4] K. Oh,[39] A. Ohlson,[57] V. Okorokov,[30] E. W. Oldag,[48] D. L. Olvitt, Jr.,[46] M. Pachr,[13] B. S. Page,[18] S. K. Pal,[53] Y. X. Pan,[7] Y. Pandit,[10] Y. Panebratsev,[21] T. Pawlak,[54] B. Pawlik,[34] H. Pei,[9] C. Perkins,[5] W. Peryt,[54] P. Pile,[4] M. Planinic,[58] J. Pluta,[54] N. Poljak,[58] J. Porter,[26] A. M. Poskanzer,[26] N. K. Pruthi,[35] M. Przybycien,[1] P. R. Pujahari,[17] J. Putschke,[56] H. Qiu,[26] A. Quintero,[22] S. Ramachandran,[23] R. Raniwala,[40] S. Raniwala,[40] R. L. Ray,[48] C. K. Riley,[57] H. G. Ritter,[26] J. B. Roberts,[41] O. V. Rogachevskiy,[21] J. L. Romero,[6] J. F. Ross,[12] A. Roy,[53] L. Ruan,[4] J. Rusnak,[14] O. Rusnakova,[13] N. R. Sahoo,[47] P. K. Sahu,[16] I. Sakrejda,[26] S. Salur,[26] J. Sandweiss,[57] E. Sangaline,[6] A. Sarkar,[17] J. Schambach,[48] R. P. Scharenberg,[38] A. M. Schmah,[26] W. B. Schmidke,[4] N. Schmitz,[28] J. Seger,[12] P. Seyboth,[28] N. Shah,[7] E. Shahaliev,[21] P. V. Shanmuganathan,[22] M. Shao,[42] B. Sharma,[35] W. Q. Shen,[44] S. S. Shi,[26] Q. Y. Shou,[44] E. P. Sichtermann,[26] R. N. Singaraju,[53] M. J. Skoby,[18] D. Smirnov,[4] N. Smirnov,[57] D. Solanki,[40] P. Sorensen,[4] H. M. Spinka,[2] B. Srivastava,[38] T. D. S. Stanislaus,[52] J. R. Stevens,[27] R. Stock,[15] M. Strikhanov,[30] B. Stringfellow,[38] M. Sumbera,[14] X. Sun,[26] X. M. Sun,[26] Y. Sun,[42] Z. Sun,[25] B. Surrow,[46] D. N. Svirida,[19] T. J. M. Symons,[26] M. A. Szelezniak,[26] J. Takahashi,[8] A. H. Tang,[4] Z. Tang,[42] T. Tarnowsky,[29] J. H. Thomas,[26] A. R. Timmins,[49] D. Tlusty,[14] M. Tokarev,[21] S. Trentalange,[7] R. E. Tribble,[47] P. Tribedy,[53] B. A. Trzeciak,[13] O. D. Tsai,[7] J. Turnau,[34] T. Ullrich,[4] D. G. Underwood,[2] G. Van Buren,[4] G. van Nieuwenhuizen,[27] M. Vandenbroucke,[46] J. A. Vanfossen, Jr.,[22] R. Varma,[17] G. M. S. Vasconcelos,[8] A. N. Vasiliev,[37] R. Vertesi,[14] F. Videbæk,[4] Y. P. Viyogi,[53] S. Vokal,[21] A. Vossen,[18] M. Wada,[48] F. Wang,[38] G. Wang,[7] H. Wang,[4] J. S. Wang,[25] X. L. Wang,[42] Y. Wang,[50] Y. Wang,[10] G. Webb,[23] J. C. Webb,[4] G. D. Westfall,[29] H. Wieman,[26] S. W. Wissink,[18] R. Witt,[51] Y. F. Wu,[9] Z. Xiao,[50] W. Xie,[38] K. Xin,[41] H. Xu,[25] J. Xu,[9] N. Xu,[26] Q. H. Xu,[43] Y. Xu,[42] Z. Xu,[4] W. Yan,[50] C. Yang,[42] Y. Yang,[25] Y. Yang,[9] Z. Ye,[10] P. Yepes,[41] L. Yi,[38] K. Yip,[4] I-K. Yoo,[39] N. Yu,[9] Y. Zawisza,[42] H. Zbroszczyk,[54] W. Zha,[42] J. B. Zhang,[9] J. L. Zhang,[43] S. Zhang,[44] X. P. Zhang,[50] Y. Zhang,[42] Z. P. Zhang,[42] F. Zhao,[7] J. Zhao,[9] C. Zhong,[44] X. Zhu,[50] Y. H. Zhu,[44] Y. Zoulkarneeva,[21] and M. Zyzak[15]

(STAR Collaboration)

[1]*AGH University of Science and Technology, Cracow, Poland*
[2]*Argonne National Laboratory, Argonne, Illinois 60439, USA*
[3]*University of Birmingham, Birmingham, United Kingdom*
[4]*Brookhaven National Laboratory, Upton, New York 11973, USA*
[5]*University of California, Berkeley, California 94720, USA*
[6]*University of California, Davis, California 95616, USA*
[7]*University of California, Los Angeles, California 90095, USA*
[8]*Universidade Estadual de Campinas, Sao Paulo, Brazil*
[9]*Central China Normal University (HZNU), Wuhan 430079, China*
[10]*University of Illinois at Chicago, Chicago, Illinois 60607, USA*
[11]*Cracow University of Technology, Cracow, Poland*
[12]*Creighton University, Omaha, Nebraska 68178, USA*
[13]*Czech Technical University in Prague, FNSPE, Prague 115 19, Czech Republic*

[14]*Nuclear Physics Institute AS CR, 250 68 Řež/Prague, Czech Republic*
[15]*Frankfurt Institute for Advanced Studies FIAS, Germany*
[16]*Institute of Physics, Bhubaneswar 751005, India*
[17]*Indian Institute of Technology, Mumbai, India*
[18]*Indiana University, Bloomington, Indiana 47408, USA*
[19]*Alikhanov Institute for Theoretical and Experimental Physics, Moscow, Russia*
[20]*University of Jammu, Jammu 180001, India*
[21]*Joint Institute for Nuclear Research, Dubna 141 980, Russia*
[22]*Kent State University, Kent, Ohio 44242, USA*
[23]*University of Kentucky, Lexington, Kentucky, 40506-0055, USA*
[24]*Korea Institute of Science and Technology Information, Daejeon, Korea*
[25]*Institute of Modern Physics, Lanzhou, China*
[26]*Lawrence Berkeley National Laboratory, Berkeley, California 94720, USA*
[27]*Massachusetts Institute of Technology, Cambridge, Massachusetts 02139-4307, USA*
[28]*Max-Planck-Institut für Physik, Munich, Germany*
[29]*Michigan State University, East Lansing, Michigan 48824, USA*
[30]*Moscow Engineering Physics Institute, Moscow, Russia*
[31]*National Institute of Science Education and Research, Bhubaneswar 751005, India*
[32]*Ohio State University, Columbus, Ohio 43210, USA*
[33]*Old Dominion University, Norfolk, Virginia 23529, USA*
[34]*Institute of Nuclear Physics PAN, Cracow, Poland*
[35]*Panjab University, Chandigarh 160014, India*
[36]*Pennsylvania State University, University Park, Pennsylvania 16802, USA*
[37]*Institute of High Energy Physics, Protvino, Russia*
[38]*Purdue University, West Lafayette, Indiana 47907, USA*
[39]*Pusan National University, Pusan, Republic of Korea*
[40]*University of Rajasthan, Jaipur 302004, India*
[41]*Rice University, Houston, Texas 77251, USA*
[42]*University of Science and Technology of China, Hefei 230026, China*
[43]*Shandong University, Jinan, Shandong 250100, China*
[44]*Shanghai Institute of Applied Physics, Shanghai 201800, China*
[45]*SUBATECH, Nantes, France*
[46]*Temple University, Philadelphia, Pennsylvania 19122, USA*
[47]*Texas A&M University, College Station, Texas 77843, USA*
[48]*University of Texas, Austin, Texas 78712, USA*
[49]*University of Houston, Houston, Texas 77204, USA*
[50]*Tsinghua University, Beijing 100084, China*
[51]*United States Naval Academy, Annapolis, Maryland, 21402, USA*
[52]*Valparaiso University, Valparaiso, Indiana 46383, USA*
[53]*Variable Energy Cyclotron Centre, Kolkata 700064, India*
[54]*Warsaw University of Technology, Warsaw, Poland*
[55]*University of Washington, Seattle, Washington 98195, USA*
[56]*Wayne State University, Detroit, Michigan 48201, USA*
[57]*Yale University, New Haven, Connecticut 06520, USA*
[58]*University of Zagreb, Zagreb HR-10002, Croatia*

(Received 7 February 2014; revised manuscript received 19 September 2014; published 9 December 2014)

We report on the first measurement of the azimuthal anisotropy (v_2) of dielectrons (e^+e^- pairs) at mid-rapidity from $\sqrt{s_{NN}} = 200$ GeV Au + Au collisions with the STAR detector at the Relativistic Heavy Ion Collider (RHIC), presented as a function of transverse momentum (p_T) for different invariant-mass regions. In the mass region $M_{ee} < 1.1$ GeV/c^2 the dielectron v_2 measurements are found to be consistent with expectations from π^0, η, ω, and ϕ decay contributions. In the mass region $1.1 < M_{ee} < 2.9$ GeV/c^2, the measured dielectron v_2 is consistent, within experimental uncertainties, with that from the $c\bar{c}$ contributions.

DOI: 10.1103/PhysRevC.90.064904 PACS number(s): 25.75.Cj, 25.75.Ld

I. INTRODUCTION

Dileptons are among the most essential tools for investigating the strongly interacting matter created in ultrarelativistic heavy-ion collisions [1,2]. Once produced, leptons, like photons, are not affected by the strong interaction. Unlike photons, however, dileptons have an additional kinematic dimension: their invariant mass. Different kinematics of lepton pairs [mass and transverse momentum (p_T) ranges] can selectively probe

the properties of the created matter throughout the whole evolution [3,4].

In the low invariant mass range of produced lepton pairs ($M_{ll} < 1.1$ GeV/c^2), vector mesons such as $\rho(770)$, $\omega(782)$, and $\phi(1020)$ and Dalitz decays of pseudoscalar mesons (π^0 and η) dominate the spectrum. In-medium properties of the spectral functions of these vector mesons may exhibit modifications related to possible chiral symmetry restoration [3,4], which can be studied via their dilepton decays. At the Super Proton Synchrotron (SPS), the low-mass dilepton enhancement in the CERES e^+e^- data [5] and in the NA60 $\mu^+\mu^-$ data [6] could be attributed to substantial medium modification of the ρ-meson spectral function. Two different realizations of chiral symmetry restoration were proposed: a dropping-mass scenario [7] and a broadening of the ρ spectral function [8], both of which described the CERES data. The precise NA60 measurement has provided a decisive discrimination between the two scenarios, with only the broadened spectral function [9] being able to describe the data.

At the Relativistic Heavy Ion Collider (RHIC), a significant enhancement in the dielectron continuum, compared to expectations from hadronic sources for $0.15 < M_{ee} < 0.75$ GeV/c^2, was observed by the PHENIX Collaboration in Au + Au collisions at $\sqrt{s_{NN}} = 200$ GeV [10]. This enhancement is reported to increase from peripheral to central Au + Au collisions and has a strong p_T dependence. At low p_T (below 1 GeV/c), the enhancement factor increases from $1.5 \pm 0.3^{\text{stat}} \pm 0.5^{\text{syst}} \pm 0.3^{\text{model}}$ in 60–92% peripheral Au + Au collisions to $7.6 \pm 0.5^{\text{stat}} \pm 1.3^{\text{syst}} \pm 1.5^{\text{model}}$ in 0–10% central Au + Au collisions. The last error is an estimate of the uncertainty in the extracted yield due to known hadronic sources. The STAR Collaboration recently reported dielectron spectra in Au + Au collisions at $\sqrt{s_{NN}} = 200$ GeV, demonstrating an enhancement with respect to the contributions from known hadronic sources in the low-mass region that bears little centrality dependence [11]. Theoretical calculations [12–14], which describe the SPS dilepton data, fail to consistently describe the low-p_T and low-mass enhancement observed by PHENIX in 0–10% and 10–20% central Au + Au collisions [10]. The same calculations, however, describe the STAR measurement of the low-p_T and low-mass enhancement from peripheral to central Au + Au collisions [11].

For $1 < p_T < 5$ GeV/c and in the mass region $M_{ee} < 0.3$ GeV/c^2, the PHENIX Collaboration derived direct photon yields through dielectron measurements to assess thermal radiation at RHIC [15]. The excess of direct photon yield in central Au + Au collisions over that observed in $p + p$ collisions is found to fall off exponentially with p_T with an inverse slope of 220 MeV/c. In addition, the azimuthal anisotropy v_2, the second harmonic of the azimuthal distribution with respect to the event plane [16], has been measured for direct photons using an electromagnetic calorimeter and found to be substantial and comparable to the v_2 for hadrons for $1 < p_T < 4$ GeV/c [17]. Model calculations for thermal photons from the quark-gluon plasma (QGP) in this kinematic region significantly underpredict the observed v_2, while the model calculations which include a significant contribution from the hadronic sources at a later stage describe the excess of the spectra and the substantial v_2 for $1 < p_T < 4$ GeV/c reasonably well [18]. With their augmented kinematics, dilepton v_2 measurements have been proposed as an alternative study of medium properties [19]. Specifically, the v_2 as a function of p_T in different invariant mass regions will enable us to probe the properties of the medium at different stages, from QGP to hadron-gas dominated.

The dilepton spectra in the intermediate mass range ($1.1 < M_{ll} < 3.0$ GeV/c^2) are expected to be related to the QGP thermal radiation [3,4]. However, contributions from other sources have to be measured experimentally, e.g., electron or muon pairs from semileptonic decays of open charm or bottom hadrons ($c + \bar{c} \to l^+ + l^- X$ or $b + \bar{b} \to l^+ + l^- X$). Utilizing dielectrons, the PHENIX Collaboration obtained the charm and bottom cross sections in $p + p$ collisions at $\sqrt{s} = 200$ GeV [20].

With the installation of a time-of-flight (TOF) detector [21], as well as an upgrade of the data acquisition system [22], the STAR detector with its large acceptance provides excellent electron identification capability at low momentum for dielectron analyses [23].

In this paper, we present the first dielectron v_2 measurements from low to intermediate mass ($M_{ee} < 2.9$ GeV/c^2) in Au + Au collisions at $\sqrt{s_{NN}} = 200$ GeV. This paper is organized as follows. Section II describes the detector and data samples used in the analysis. Sections III A and III B describe the electron identification, electron pair distributions, and background subtraction. Sections III C and III D describe the analysis details of the azimuthal anisotropy and simulation. Section IV describes the systematic uncertainties. Results for the centrality, mass, and p_T dependence of dielectron v_2 are presented in detail in Sec. V. Lastly, Sec. VI provides a concluding summary.

II. DETECTOR AND DATA SAMPLE

The two main detectors used in this analysis are the Time Projection Chamber (TPC) [24] and the TOF detector. Both have full azimuthal coverage at mid-rapidity. The TPC is STAR's main tracking detector, measuring momentum, charge, and energy loss of charged particles. The ionization energy loss (dE/dx) of charged particles in the TPC gas is used for particle identification [25,26]. In addition, the TOF detector extends STAR's hadron identification capabilities to higher momenta and significantly improves its electron identification capabilities [27,28].

The data used for this analysis were taken in 2010 and 2011. A total of 760 million minimum-bias events, with 240 million from 2010 and 520 million from 2011 data samples of $\sqrt{s_{NN}} =$ 200 GeV Au + Au collisions were used in the analysis. These events were required to have collision vertices within 30 cm of the TPC center along the beam line, where the material budget is minimal (0.6% in radiation length in front of the TPC inner field cage). The minimum-bias trigger was defined by the coincidence of signals from the two Vertex Position Detectors (VPDs) [29], located on each side of the STAR barrel, covering a pseudorapidity range of $4.4 < |\eta| < 4.9$. The centrality tagging was determined by the measured charged particle multiplicity density in the TPC within $|\eta| < 0.5$ [30]. The 2010 and 2011 minimum-bias data (0–80% centrality) were

TABLE I. Criteria used for the selection of tracks for electron identification. NFit is the number of points used to fit the TPC track, and NMax is the maximum possible number for that track. dE/dx points is the number of points used to derive the dE/dx value. The DCA is the distance of the closest approach between the trajectory of a particle and the collision vertex.

$\|\eta\|$	<1
p_T	>0.2 GeV/c
DCA	<1 cm
NFit	>19
NFit / NMax	>0.52
dE/dx points	>15

analyzed separately. The dielectron v_2 measurement in this article is the combined v_2 result from these two data sets.

III. DATA ANALYSIS

A. Electron identification

Particles directly originating from the collision, with trajectories that project back to within 1 cm of the collision vertex, calculated in three dimensions, were selected for this analysis. Table I lists selection criteria for the tracks for further electron identification. The normalized dE/dx ($n\sigma_e$) is defined as $n\sigma_e = \ln(dE/dx/I_e)/R_e$, where dE/dx is the measured energy loss of a particle, and I_e is the expected dE/dx of an electron. R_e is the resolution of $\ln(dE/dx/I_e)$, defined as the width of its distribution, and is better than 8% for these data. Figure 1(a) shows the $n\sigma_e$ distribution as a function of momentum from the TPC, while panel (b) shows the inverse velocity $1/\beta$ measurements from the TOF versus the momentum measured by the TPC. Panel (c) shows the $n\sigma_e$ distribution versus momentum with the requirement on velocity that $|1/\beta - 1/\beta_{\rm exp}| < 0.025$, in which $\beta_{\rm exp}$ is the velocity calculated with the assumption of electron mass. Panel (d) presents the $n\sigma_e$ distribution for $0.68 < p_T < 0.73$ GeV/c after the cut $|1/\beta - 1/\beta_{\rm exp}| < 0.025$ is applied. With perfect calibration, the $n\sigma_e$ for single electrons should follow a standard normal distribution. Electron candidates whose $n\sigma_e$ falls between the lines in Fig. 1(c) are selected. From the multiple-component fit to the dE/dx distribution, an example of which is shown in panel (d), one can obtain the purity of electron candidates. The purity is 95% on average and depends on momentum [11], as shown in Fig. 2. With the combined information of velocity (β) from the TOF and dE/dx from the TPC, electrons can be clearly identified from low to intermediate p_T ($0.2 < p_T < 3$ GeV/c) for $|\eta| < 1$ [31,32]. This is important for dielectron measurements from the low to intermediate mass region.

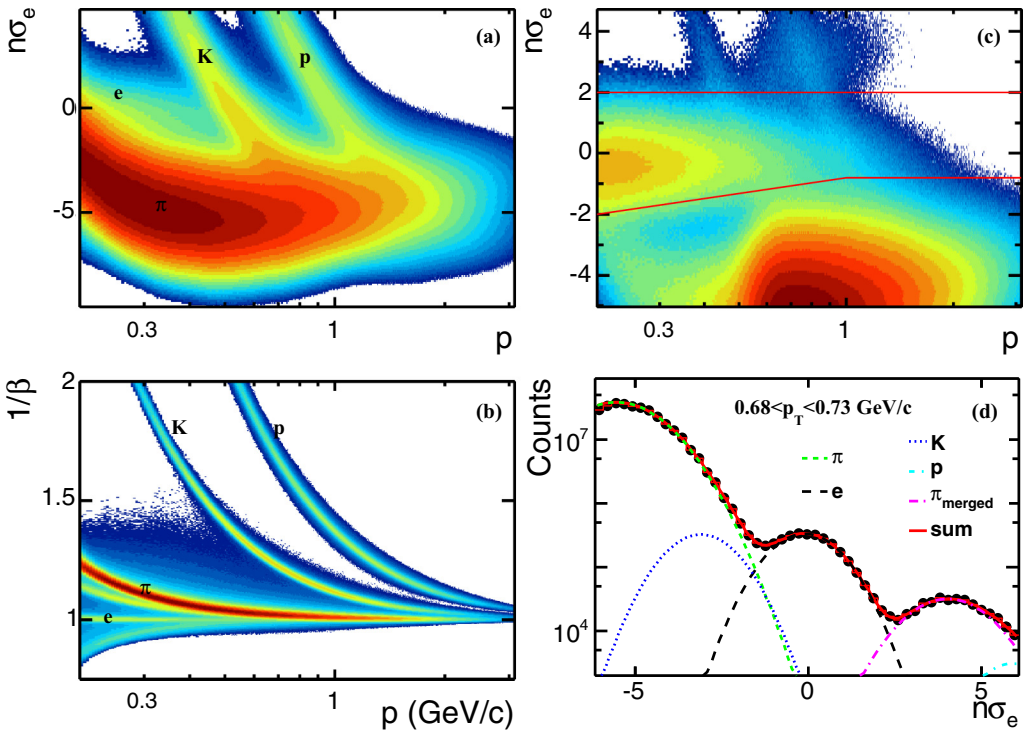

FIG. 1. (Color online) (a) The normalized dE/dx distribution as a function of momentum from TPC in Au + Au collisions at $\sqrt{s_{NN}} = 200$ GeV. (b) $1/\beta$ measurements from TOF versus the momentum from TPC in Au + Au collisions. The $1/\beta$ resolution is 0.011. (c) The normalized dE/dx distribution as a function of momentum with the cut of $|1/\beta - 1/\beta_{\rm exp}| < 0.025$. An electron band is prominent with the requirement of velocity close to the speed of light from the TOF measurement. Electron candidates whose $n\sigma_e$ falls between the lines are selected for further dielectron analysis. (d) The $n\sigma_e$ distribution for $0.68 < p_T < 0.73$ GeV/c after the cut $|1/\beta - 1/\beta_{\rm exp}| < 0.025$ is applied. The solid curve represents a multiple Gaussian fit to the $n\sigma_e$ distribution. Different components from the fit are also shown. The $\pi_{\rm merged}$ represents contribution from two merged π tracks.

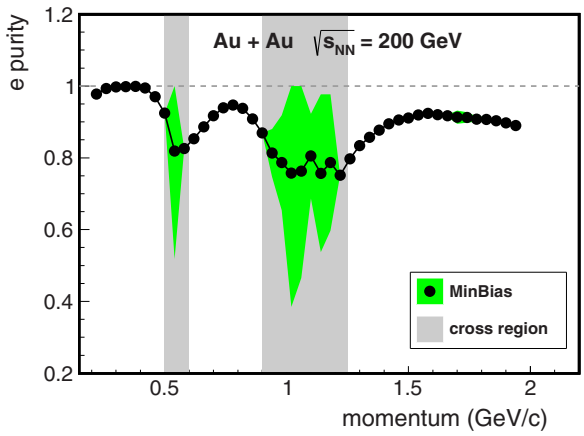

FIG. 2. (Color online) The purity of electron candidates as a function of momentum in minimum-bias Au + Au collisions at $\sqrt{s_{NN}} = 200$ GeV. In the cross regions, the electron candidates overlap with hadron components in the dE/dx distribution, which results in large uncertainties in the multi-component fit, as shown by the shading around the data points.

B. Dielectron invariant mass distribution and background subtraction

The dielectron signals may come from decays of both light-flavor and heavy-flavor hadrons. The light-flavor sources include π^0, η, and η' Dalitz decays: $\pi^0 \to \gamma e^+e^-$, $\eta \to \gamma e^+e^-$, and $\eta' \to \gamma e^+e^-$; and vector meson decays: $\omega \to \pi^0 e^+e^-$, $\omega \to e^+e^-$, $\rho^0 \to e^+e^-$, $\phi \to \eta e^+e^-$, and $\phi \to e^+e^-$. The heavy-flavor sources include $J/\psi \to e^+e^-$ and heavy-flavor hadron semileptonic decays: $c\bar{c} \to e^+e^-$ and $b\bar{b} \to e^+e^-$. The signals also include Drell-Yan contributions. The dielectron contributions from photon conversions ($\gamma \to e^+e^-$) in the detector material are present in the raw data. The momenta of these electrons are biased, which results in a multiple-peak structure in the dielectron mass distribution for $M_{ee} < 0.12$ GeV/c^2. The peak position in the mass distribution depends on the conversion point in the detector [33]. It is found that the dielectron v_2 from photon conversions is the same as that from π^0 Dalitz decays. The vector meson contributions to the Au + Au data may be modified in the medium. QGP thermal radiation and additional contributions from the hadron gas would also be contained in the data.

With high-purity electron samples, the e^+e^- pairs from each event are accumulated to generate the invariant mass distributions (M_{ee}), here referred to as the unlike-sign distributions. The unlike-sign distributions contain both signal (defined in the previous paragraph) and backgrounds of random combinatorial pairs and correlated cross pairs. The correlated cross pairs come from two e^+e^- pairs from a single meson decay: a Dalitz decay followed by a conversion of the decay photon, or conversions of multiple photons from the same meson. The electron candidates are required to be in the range $|\eta| < 1$ and $p_T > 0.2$ GeV/c, while the rapidity of e^+e^- pairs (y_{ee}) is required to be in the region $|y_{ee}| < 1$.

Two methods are used for background estimation, based on same-event like-sign and mixed-event unlike-sign techniques. In the mixed-event technique, tracks from different events are used to form unlike-sign or like-sign pairs. The events are divided into 9000 categories according to the collision vertex (10 bins), event plane (defined in Sec. III C) azimuthal angle (100 bins from 0 to $\pi/2$), and centrality (9 bins). The two events to be mixed must come from the same event category to ensure similar detector geometric acceptance, azimuthal anisotropy, and track multiplicities. We find that when the number of event plane bins is larger than or equal to 30, the mixed-event spectrum describes the combinatorial background.

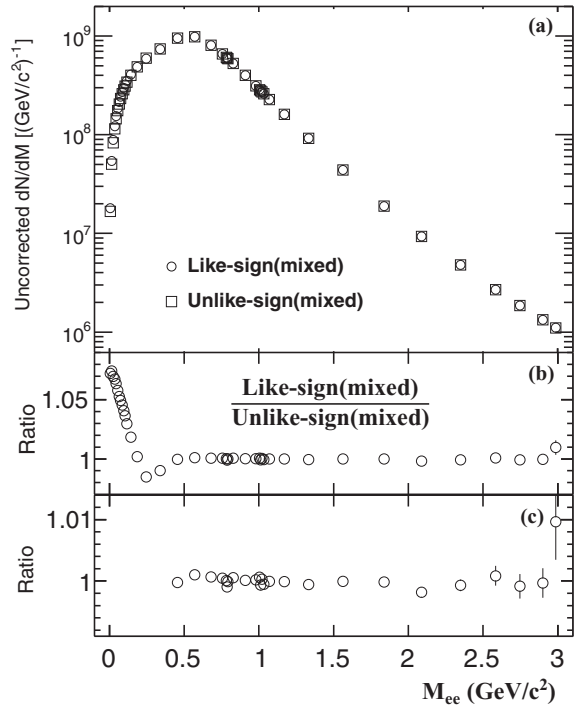

FIG. 3. (a) The mixed-event unlike-sign and mixed-event like-sign electron pair invariant mass distributions in minimum-bias Au + Au collisions at $\sqrt{s_{NN}} = 200$ GeV. (b) The ratio of mixed-event like-sign distribution to mixed-event unlike-sign distribution in minimum-bias Au + Au collisions at $\sqrt{s_{NN}} = 200$ GeV. (c) A zoom-in version of panel (b).

In the same-event like-sign technique, electrons with the same charge sign from the same events are paired. Due to the sector structure of the TPC, and the different bending directions of positively and negatively charged particle tracks in the transverse plane, like-sign and unlike-sign pairs have different acceptances. The correction for this acceptance difference is applied to the same-event like-sign pair distribution before background subtraction. The acceptance difference between same-event unlike-sign and same-event like-sign pairs is obtained using the mixed-event technique. Figure 3(a) shows the mixed-event unlike-sign and mixed-event like-sign electron pair invariant mass distributions in $\sqrt{s_{NN}} = 200$ GeV minimum-bias Au + Au collisions. The ratio of these two distributions, the acceptance difference factor, is shown in Fig. 3(b), and its zoom-in version is shown in Fig. 3(c). The centrality and p_T dependences are presented in Figs. 4 and 5, respectively. These figures show that the acceptance

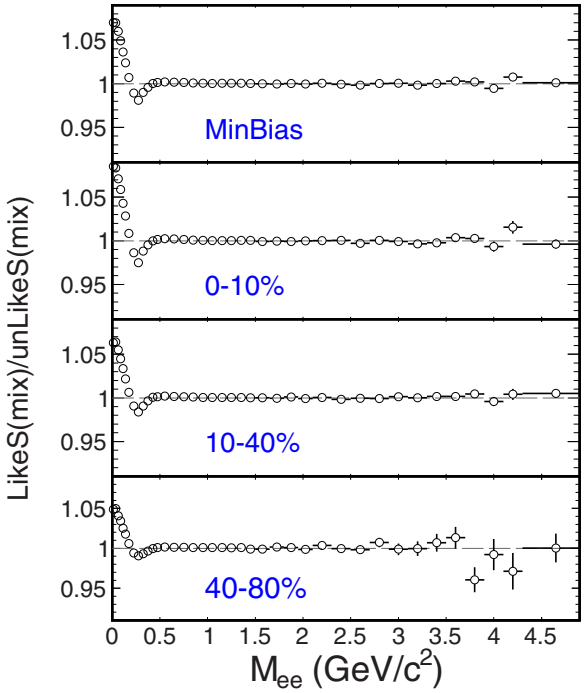

FIG. 4. (Color online) The ratio of the mixed-event like-sign distribution to the mixed-event unlike-sign distribution in minimum-bias Au + Au collisions at $\sqrt{s_{NN}} = 200$ GeV, as well as specific centrality selections of the collisions.

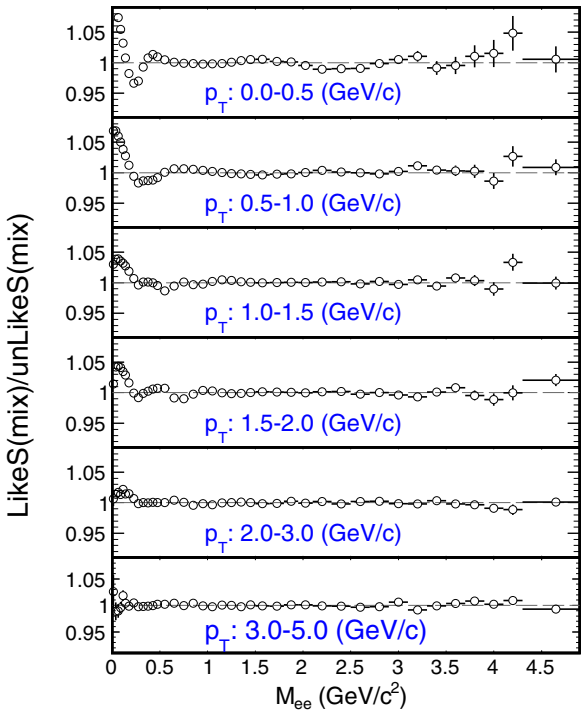

FIG. 5. (Color online) The ratio of the mixed-event like-sign distribution to the mixed-event unlike-sign distribution in different p_T ranges in minimum-bias Au + Au collisions at $\sqrt{s_{NN}} = 200$ GeV.

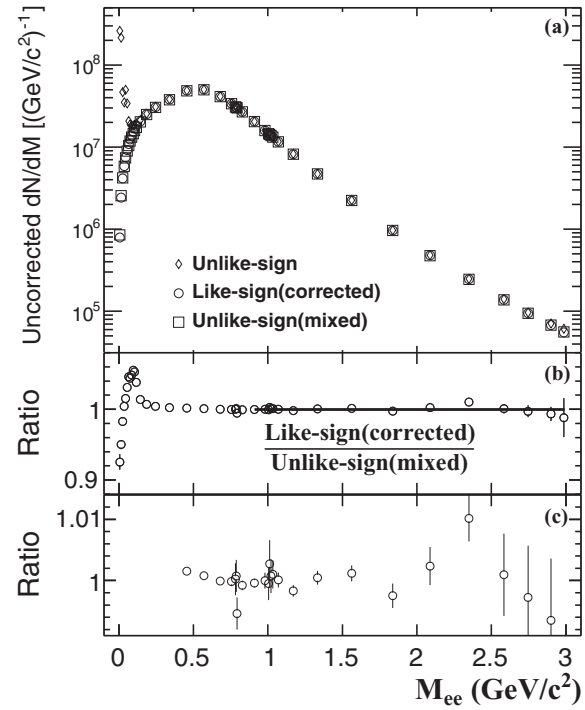

FIG. 6. (a) The electron pair invariant mass distributions for same-event unlike-sign pairs, same-event like-sign pairs, and mixed-event unlike-sign pairs in minimum-bias Au + Au collisions at $\sqrt{s_{NN}} = 200$ GeV. The electron candidates are required to be in the range $|\eta| < 1$ and have p_T greater than 0.2 GeV/c. The ee pairs are required to be in the rapidity range $|y_{ee}| < 1$. Variable bin widths are used for the yields and signal-to-background ratios. (b) The ratio of the same-event like-sign distribution (corrected for the acceptance difference) to the normalized mixed-event unlike-sign distribution in minimum-bias Au + Au collisions at $\sqrt{s_{NN}} = 200$ GeV. (c) A zoom-in version of panel (b).

differences at low invariant mass are largest at low p_T and in the most central collisions.

After correcting for the acceptance difference, the same-event like-sign distribution is compared to the same-event unlike-sign pair distribution (which contains the signal) and the mixed-event unlike-sign pair distribution in Fig. 6(a). The mixed-event unlike-sign distribution is normalized to match the same-event like-sign distribution in the mass region 0.9–3.0 GeV/c^2. For $M_{ee} > 0.9$ GeV/c^2, the ratio of the same-event like-sign distribution over the normalized mixed-event unlike-sign distribution is found constant with χ^2/NDF of 15/16, as shown in Fig. 6(b). The constant is 0.9999 ± 0.0004. The zoom-in version, centrality dependence, and p_T dependence of this ratio are shown in Figs. 6(c), 7, and 8, respectively. In addition, the centrality and p_T dependences of the ratio of the same-event like-sign distribution over the normalized mixed-event like-sign distribution are presented in Figs. 9 and 10, respectively.

In the low-mass region, the correlated cross-pair background is present in the same-event like-sign distribution, but not in the mixed-event unlike-sign background. In the higher mass region, the mixed-event unlike-sign distribution

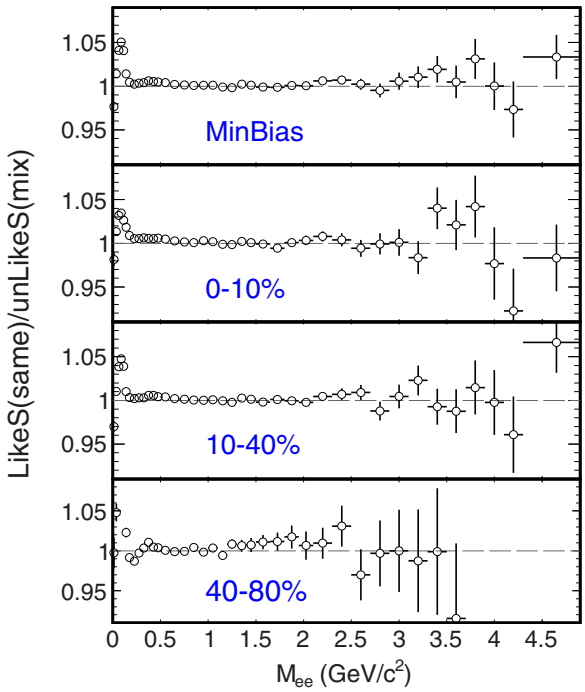

FIG. 7. (Color online) The centrality dependence of the ratio of the same-event like-sign distribution (corrected for the acceptance difference) to the normalized mixed-event unlike-sign distribution in minimum-bias Au + Au collisions at $\sqrt{s_{NN}} = 200$ GeV.

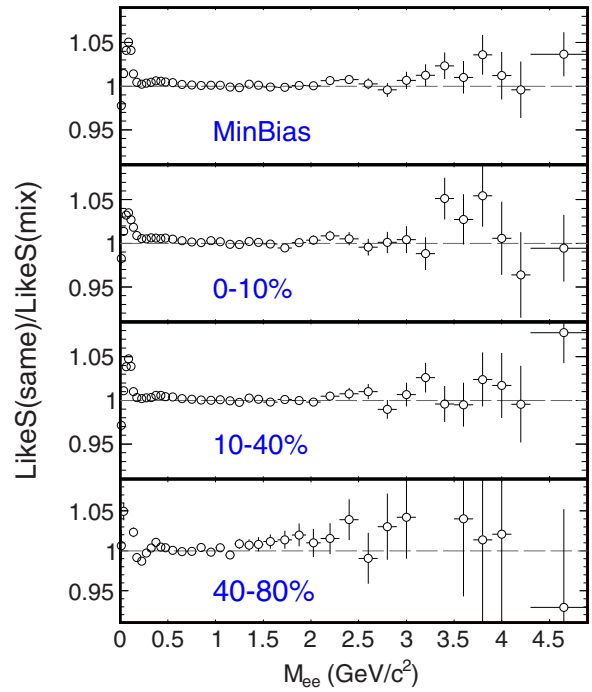

FIG. 9. (Color online) The centrality dependence of the ratio of the same-event like-sign distribution to the normalized mixed-event like-sign distribution in minimum-bias Au + Au collisions at $\sqrt{s_{NN}} = 200$ GeV.

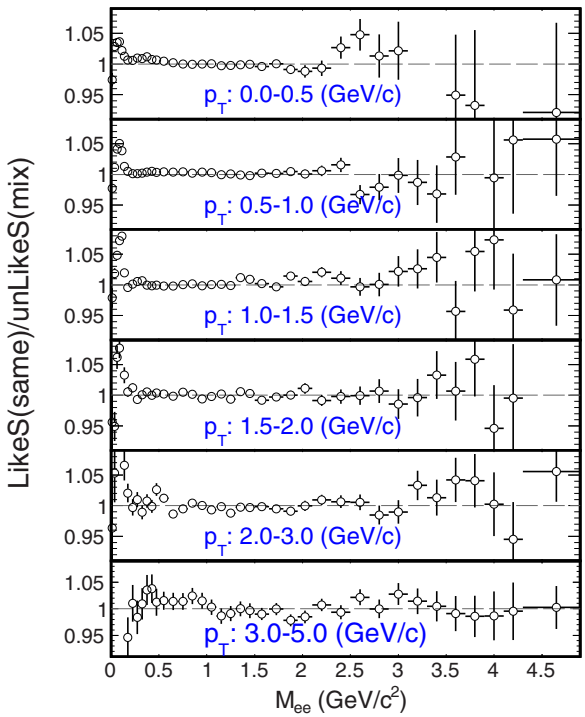

FIG. 8. (Color online) The p_T dependence of the ratio of the same-event like-sign distribution (corrected for the acceptance difference) to the normalized mixed-event unlike-sign distribution in minimum-bias Au + Au collisions at $\sqrt{s_{NN}} = 200$ GeV.

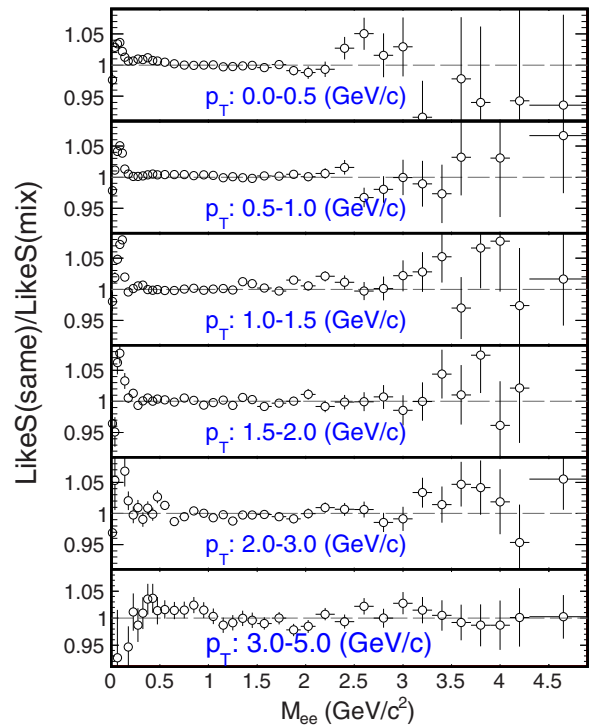

FIG. 10. (Color online) The p_T dependence of the ratio of the same-event like-sign distribution to the normalized mixed-event like-sign distribution in minimum-bias Au + Au collisions at $\sqrt{s_{NN}} = 200$ GeV.

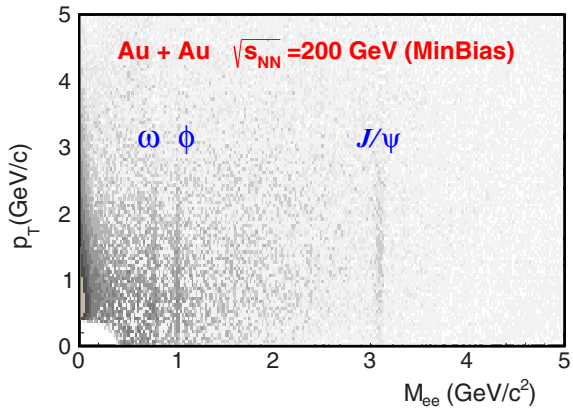

FIG. 11. (Color online) The p_T as a function of M_{ee} for dielectron signal without efficiency correction in $\sqrt{s_{NN}} = 200$ GeV minimum-bias Au + Au collisions.

matches the same-event like-sign distribution. Therefore, for $M_{ee} < 0.9$ GeV/c^2 like-sign pairs from the same events are used for background subtraction. For $M_{ee} > 0.9$ GeV/c^2 we subtract the mixed-event unlike-sign background to achieve better statistical precision.

Figure 11 shows the p_T as a function of M_{ee} for the dielectron continuum after background subtraction without efficiency correction in $\sqrt{s_{NN}} = 200$ GeV minimum-bias Au + Au collisions. Figure 12(a) shows the dielectron-signal mass distribution in minimum-bias Au + Au collisions at $\sqrt{s_{NN}} = 200$ GeV. The analysis requires $|y_{e^+e^-}| < 1, |\eta_e| < 1$ and $p_T(e) > 0.2$ GeV/c. The distribution is not corrected for efficiency. The signal-to-background (S/B) ratio in Au + Au collisions versus M_{ee} is shown in Fig. 12(b).

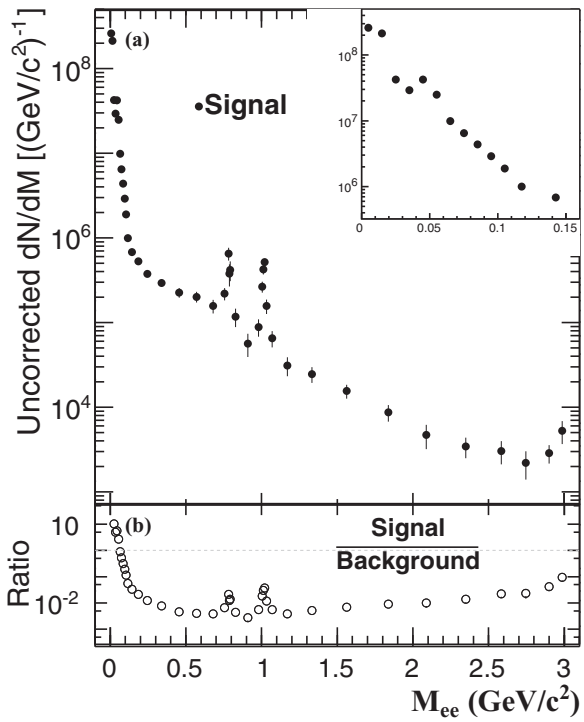

FIG. 12. (a) The dielectron continuum without efficiency correction in $\sqrt{s_{NN}} = 200$ GeV minimum-bias Au + Au collisions. The two-peak structure, as shown in the inset, for $M_{ee} < 0.12$ GeV/c^2 is due to photon conversions in the beam pipe and supporting structure. Errors are statistical only. (b) The signal-over-background ratio in $\sqrt{s_{NN}} = 200$ GeV minimum-bias Au + Au collisions. The first two data points are not shown for clarity. Errors are statistical.

C. Method to obtain azimuthal anisotropy

Hydrodynamic flow of produced particles leads to azimuthal correlations among particles relative to the reaction plane [16]. However, the measured correlations also include effects not related to reaction plane orientation. These are usually referred to as nonflow, and are due to, for example, resonance decays and parton fragmentation. In this analysis, we use the "event-plane" method to determine the azimuthal anisotropy of produced dielectrons [16].

The event plane is reconstructed using tracks from the TPC. The event flow vector Q_2 and the event-plane angle Ψ_2 are defined by [16]

$$Q_2 \cos(2\Psi_2) = Q_{2x} = \sum_i w_i \cos(2\phi_i), \tag{1}$$

$$Q_2 \sin(2\Psi_2) = Q_{2y} = \sum_i w_i \sin(2\phi_i), \tag{2}$$

$$\Psi_2 = \left(\tan^{-1}\frac{Q_{2y}}{Q_{2x}}\right)\Big/2, \tag{3}$$

where the summation is over all particles i used for event-plane determination. Here, ϕ_i and w_i are measured azimuthal angle and weight for the particle i, respectively. The weight w_i is equal to the particle p_T up to 2 GeV/c, and is kept constant at higher p_T. The electron candidates are excluded in the event-plane reconstruction to avoid the self-correlation effect. A PYTHIA study indicates that decay kaons from heavy flavor have no additional effect on event-plane determination. An azimuthally nonhomogeneous acceptance or efficiency of the detectors can introduce a bias in the event-plane reconstruction which would result in a nonuniform Ψ_2 angle distribution in the laboratory coordinate system. The recentering and shifting methods [34,35] were used to flatten the Ψ_2 distribution.

The observed v_2 is the second harmonic of the azimuthal distribution of particles with respect to the event plane:

$$v_2^{\rm obs} = \langle \cos[2(\phi - \Psi_2)] \rangle, \tag{4}$$

where angle brackets denote an average over all particles with azimuthal angle ϕ in a given phase space and $\phi - \Psi_2$ ranges from 0 to $\pi/2$. The electron reconstruction efficiency is independent of $\phi - \Psi_2$. The real v_2 is corrected for event-plane resolution as

$$v_2 = \frac{v_2^{\rm obs}}{C\sqrt{\langle \cos\left[2\left(\Psi_2^a - \Psi_2^b\right)\right]\rangle}}, \tag{5}$$

where Ψ_2^a and Ψ_2^b are the second-order event planes determined from different subevents, C is a constant calculated from the known multiplicity dependence of the resolution [16], and the

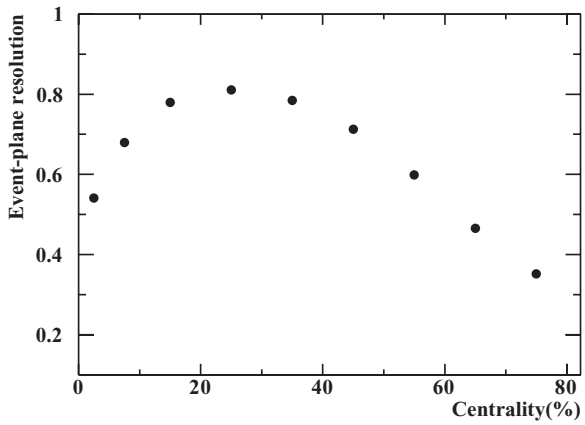

FIG. 13. The event-plane resolution from central to peripheral (left to right) collisions in minimum-bias Au + Au collisions at $\sqrt{s_{NN}} = 200$ GeV.

brackets denote an average over a large event sample. The denominator represents the event-plane resolution, which is obtained from two random subevents [36]. Figure 13 shows the event-plane resolution for different centralities in 200 GeV Au + Au collisions.

The v_2 for dielectron signals for each mass and p_T bin is obtained using the formula

$$v_2^S(M_{ee}, p_T) = \frac{v_2^{\text{total}}(M_{ee}, p_T)}{r(M_{ee}, p_T)} - \frac{1 - r(M_{ee}, p_T)}{r(M_{ee}, p_T)} v_2^B(M_{ee}, p_T), \tag{6}$$

in which v_2^S, v_2^{total}, and v_2^B represent v_2 for the dielectron signal, v_2 for the same-event unlike-sign electron pairs, and v_2 for the background electron pairs (determined through either the mixed-event unlike-sign technique or the same-event like-sign method, as discussed in the previous sections), respectively. The parameter r represents the ratio of the number of dielectron signals (N_S) to the number of the same-event unlike-sign electron pairs (N_{S+B}). The v_2^{total} is the yield-weighted average from the dielectron signal and background. The mixed-event

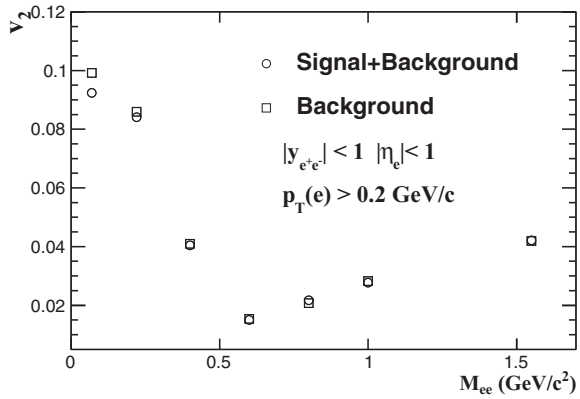

FIG. 14. The v_2 for the same-event unlike-sign electron pairs (circles) and background (squares) as a function of M_{ee} within STAR acceptance in minimum-bias Au + Au collisions at $\sqrt{s_{NN}} = 200$ GeV.

unlike-sign technique is applied for $M_{ee} > 0.9$ GeV/c^2, for which the mixed-event unlike-sign distribution for each of the $(\phi - \Psi_2)$ bins (the bin width is $\frac{\pi}{10}$) is normalized to the corresponding same-event like-sign distribution in the same $\phi - \Psi_2$ bin. For the five $(\phi - \Psi_2)$ bins, the normalization factors differ by 0.1%. Figure 14 shows v_2^{total} and v_2^B as a function of M_{ee} within the STAR acceptance in minimum-bias Au + Au collisions at $\sqrt{s_{NN}} = 200$ GeV.

D. Cocktail simulation

In the following we wish to obtain a representation of the dielectron v_2 distributions in p_T and M_{ee} by a cocktail simulation that accounts for the decays of all prominent hadronic sources. We shall obtain the dielectron v_2 from each decay component by combining the measured p_T spectra of the "mother mesons," with the previously measured v_2 distributions of these mesons.

As mentioned earlier, the dielectron pairs may come from decays of light-flavor and heavy-flavor hadrons. Contributions from the following hadronic sources and processes were included in the cocktail simulation to compare with the measured data: $\pi^0 \to \gamma e^+ e^-$, $\eta \to \gamma e^+ e^-$, $\omega \to \pi^0 e^+ e^-$, $\omega \to e^+ e^-$, $\phi \to \eta e^+ e^-$, and $\phi \to e^+ e^-$ for $M_{ee} < 1.1$ GeV/c^2. In the intermediate mass region, we simulate the dielectron v_2 from the $c\bar{c}$ correlated contribution.

The π^0 invariant yield is taken as the average of π^+ and π^- [37,38]. The ϕ yield is taken from STAR measurements [39], while the η yield is from a PHENIX measurement [40]. We fit the meson invariant yields with Tsallis functions [41], as shown in Fig. 15(a). The ω p_T-spectrum shape is derived from the Tsallis function. The ω total yield at mid-rapidity $(dN/dy|_{y=0})$ is obtained by matching the simulated cocktail to the efficiency-corrected dielectron mass spectrum in the ω peak region. Table II lists the $dN/dy|_{y=0}$ of hadrons in 200 GeV minimum-bias Au + Au collisions. In addition, we parametrize the π, K_S^0, and ϕ v_2 from previous measurements [36,42–44] with a data-driven functional form, $A\tanh(Bp_T) + C\arctan(Dp_T) + Ee^{-p_T} + Fe^{-p_T^2}$, where A, B, C, D, E, and F are fit parameters. The η and ω v_2 are assumed to be the same as K_S^0 and ϕ v_2 respectively, since the masses of the η and K_S^0 mesons, as well as those of the ω and ϕ mesons, are similar. The mass-dependent hydrodynamic behavior was observed for hadron v_2 at $p_T < 2$ GeV/c while in the range of $2 < p_T < 6$ GeV/c, the number of constituent quark scaling was observed in Au + Au collisions at $\sqrt{s_{NN}} = 200$ GeV [1,2]. Due to different methods and detector configurations, the nonflow effects vary from 3–5% for charged and neutral π measured by PHENIX to 15–20% for charged π, K_S^0, and ϕ measured by STAR. Figures 15(b)–15(d) show the previously measured meson v_2 and the fit functions.

With the Tsallis functions for the spectra and the parametrizations for v_2 as input, we simulate decays of π^0, η, ω, and ϕ with appropriate branching ratios (BRs), and obtain the dielectron v_2, as shown in Fig. 16. The final v_2 is the yield-weighted average from different contributions. The same acceptance conditions after momentum resolution smearing are utilized as those used in the analysis of real

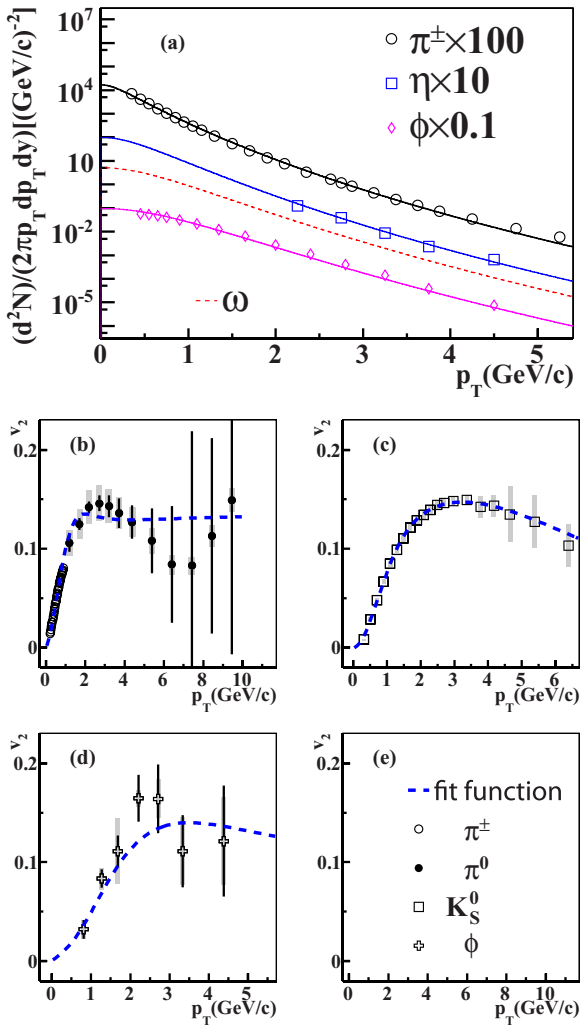

FIG. 15. (Color online) (a) The invariant yields of identified mesons, fit with Tsallis functions [41] in Au + Au collisions at $\sqrt{s_{NN}} = 200$ GeV. See text for details. (b)–(d) The v_2 of identified mesons, fit with a function for $\sqrt{s_{NN}} = 200$ GeV minimum-bias Au + Au collisions. See text for details.

events. The Kroll-Wada expression is used for the Dalitz decay: $\pi^0 \to \gamma e^+e^-$, $\eta \to \gamma e^+e^-$, $\omega \to \pi^0 e^+e^-$, and $\phi \to \eta e^+e^-$ [32,45,46].

TABLE II. The total yields at mid-rapidity (dN/dy) from the Tsallis fit and decay branching ratios of hadrons in minimum-bias Au + Au collisions at $\sqrt{s_{NN}} = 200$ GeV.

Meson	$\frac{dN}{dy}$	Relative uncertainty	Decay channel	BR
π^0	98.5	8%	γe^+e^-	1.174×10^{-2}
η	7.86	30%	γe^+e^-	7.0×10^{-3}
ω	9.87	33%	e^+e^-	7.28×10^{-5}
ω			$\pi^0 e^+e^-$	7.7×10^{-4}
ϕ	2.43	10%	e^+e^-	2.954×10^{-4}
ϕ			ηe^+e^-	1.15×10^{-4}

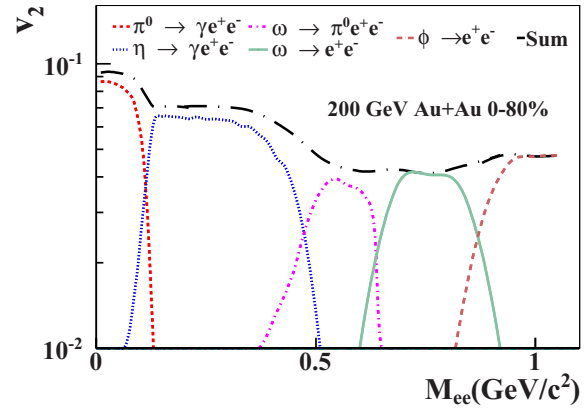

FIG. 16. (Color online) The simulated v_2 as a function of M_{ee} from π^0, η, ω, and ϕ decays within the STAR acceptance in minimum-bias Au + Au collisions at $\sqrt{s_{NN}} = 200$ GeV, including the contributions from specific decays. The contribution from $\phi \to \eta e^+e^-$ is smaller than 1% and is not shown for clarity. The bin width is 20 MeV/c^2.

In different mass regions different particle species dominate the production, as listed in Table III [11,32]. Studying v_2 in different mass regions should therefore help discern the azimuthal anisotropy of different species. Figure 16 shows that among π^0, η, ω, and ϕ decays, $\pi^0 \to \gamma e^+e^-$, $\eta \to \gamma e^+e^-$, $\omega \to \pi^0 e^+e^-$, $\omega \to e^+e^-$, and $\phi \to e^+e^-$ dominate the v_2 contribution in the mass regions [0,0.14], [0.14,0.30], [0.5,0.7], [0.76,0.80], and [0.98,1.06] GeV/c^2 respectively.

For $1.1 < M_{ee} < 2.9$ GeV/c^2, we simulate the dielectron v_2 from $c\bar{c}$ correlated contributions. To get a handle on the unknown $c\bar{c} \to e^+e^-X$ correlation in Au + Au collisions, we take two extreme approaches to simulate this v_2 contribution: (1) we assume the c and $\bar{c}$ are completely uncorrelated; (2) we assume the c and $\bar{c}$ correlation is the same as shown in PYTHIA 6.416, in which the k_T factor is set by PARP(91) = 1 GeV/c, and the parton shower is set by PARP(67) = 1 [47]. With these parameter values, PYTHIA can describe the shape of the D^0 [48] spectrum and the nonphotonic electron spectrum measured by STAR [31,49] for $p + p$ collisions.

In Fig. 17, the measured spectrum and v_2 of electrons from heavy-flavor decays [50] are shown as well as results of a parametrization which is used to obtain the dielectron v_2 from the $c\bar{c}$ contribution. We find that the dielectron v_2 from $c\bar{c}$ contribution does not show a significant difference for the two cases explained above. The v_2 value is 0.022 for the

TABLE III. The sources of dielectrons in different mass regions.

Mass region (GeV/c^2)	Dominant source(s) of dielectrons
0–0.14	π^0 and photon conversions
0.14–0.30	η
0.50–0.70	charm + ρ^0 (in-medium)
0.76–0.80	ω
0.98–1.06	ϕ
1.1–2.9	charm + thermal radiation

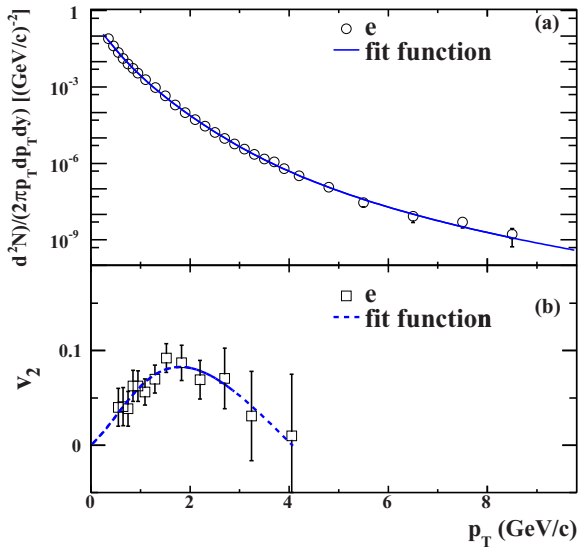

FIG. 17. (Color online) The invariant yield and v_2 of electrons from heavy flavor decays [50] fitted with functions in minimum-bias Au + Au collisions at $\sqrt{s_{NN}} = 200$ GeV. The spectrum is fit with a function $A[e^{B\sqrt{{p_T}^2+C}+D({p_T}^2+C)} + \sqrt{{p_T}^2+C}/E]^F$, where A, B, C, D, E, and F are fit parameters. The v_2 is fit with the same function as used to parametrize the meson v_2 shown in Fig. 15.

PYTHIA-correlation case and 0.027 for the uncorrelated case. Therefore, in the subsequent sections, we use the uncorrelated result to compare with our measurements. Figure 18 shows the dielectron v_2 from the $c\bar{c}$ contribution as a function of M_{ee} and p_T with a completely uncorrelated c and $\bar{c}$.

IV. SYSTEMATIC UNCERTAINTIES

The systematic uncertainties for the dielectron v_2 are dominated by background subtraction. The combinatorial background effect is evaluated by changing the DCA cut of the electron candidates. We vary the DCA cut from less than 1 cm to less than 0.8 cm so that the number of dielectron pairs changes by 20%.

The uncertainties in the correction of the acceptance difference between same-event unlike-sign and same-event like-sign pairs are studied and found to have a negligible contribution.

For $0.9 < M_{ee} < 2.9$ GeV/c^2, there are additional systematic uncertainties from the mixed-event normalization and background subtraction methods. The uncertainty on the mixed-event normalization is obtained by taking the full difference between the results from varying the normalization range from $0.9 < M_{ee} < 3.0$ to $0.7 < M_{ee} < 3.0$ GeV/c^2. In addition, there can be correlated sources in the same-event like-sign pairs for which the mixed-event background cannot completely account. This would lead to a larger v_2 for the dielectron signal when using mixed-event background subtraction. Therefore, the full difference between mixed-event unlike-sign and same-event like-sign background subtraction contributes to the lower bound of the systematic uncertainties. In the mass region 0.98–1.06 GeV/c^2, the full difference between mixed-event unlike-sign and same-event like-sign background subtraction is negligible and not shown in Table IV.

We also evaluate the hadron contamination effect by changing the $n\sigma_e$ cut. The hadron contamination is varied from 5% to 4% and to 6%. The v_2 difference between the default value and the new value is quoted as part of the systematic uncertainties, as shown in Table IV.

In addition, we use the η-subevent method [36] to study the systematic uncertainties for the dielectron v_2 in the π^0 Dalitz decay mass region. An η gap of $|\eta| < 0.3$ between positive and negative pseudorapidity subevents is introduced to reduce nonflow effects [36]. The v_2 difference between the η-subevent method and the default method contributes $(0.1–7.3) \times 10^{-3}$ absolute systematic uncertainties for $M_{ee} < 0.14$ GeV/c^2. We do not study this effect for the dielectron v_2 in the other mass regions due to limited statistics. However, the systematic uncertainty from this is expected to be much smaller than the statistical precision of the dielectron v_2.

The systematic uncertainties of dielectron v_2 for the 2010 and 2011 data sets are studied separately and found to be comparable. For the combined results, the systematic uncertainties are taken as the average from the two data sets. Table IV lists sources and their contributions to the absolute systematic uncertainties for the dielectron v_2 values in different mass regions. For each mass region, the systematic

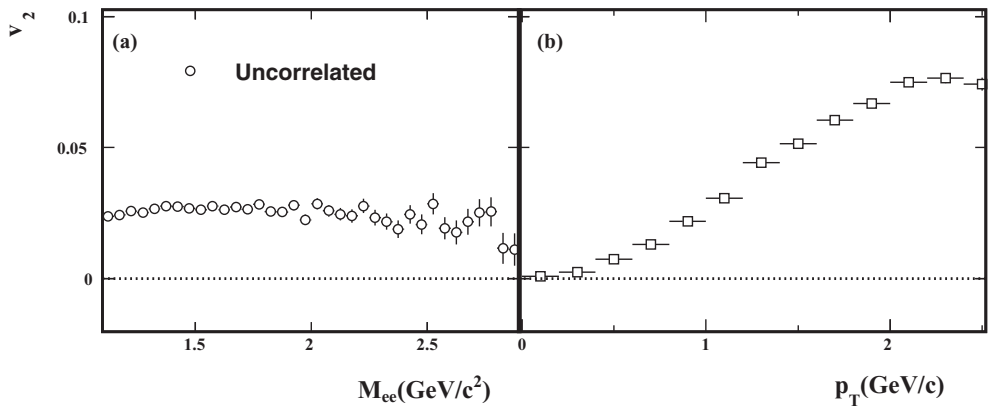

FIG. 18. The dielectron v_2 from the $c\bar{c}$ contribution as a function of M_{ee} and p_T with a completely uncorrelated c and $\bar{c}$.

TABLE IV. Sources and their contributions to the absolute systematic uncertainties for dielectron v_2 measurements in different mass regions. The uncertainties for each source are p_T dependent and listed as a range for each mass region. The total absolute systematic uncertainties are the quadratic sums of the different contributions. NR represents normalization range. bg represents background.

Source/ contribution	0–0.14	0.14–0.30	0.5–0.7	0.76–0.80	0.98–1.06	1.1–2.9 GeV/c^2
DCA cut	$(0.2–1.3)\times10^{-3}$	$(0.6–2.8)\times10^{-2}$	$(2.5–9.7)\times10^{-2}$	$(0.4–3.7)\times10^{-2}$	$(1.3–2.7)\times10^{-2}$	$(0.9–12.5)\times10^{-2}$
NR					$(1.0–3.0)\times10^{-2}$	$(3.2–6.8)\times10^{-2}$
bg method						$-(8.0–34.1)\times10^{-2}$
$n\sigma_e$ cut	$<1\times10^{-4}$	$(0.1–0.4)\times10^{-2}$	$(0.2–0.4)\times10^{-2}$	$(0.1–0.6)\times10^{-2}$	$(0.3–1.0)\times10^{-2}$	$(0.3–2.8)\times10^{-2}$
η-gap	$(0.1–7.3)\times10^{-3}$					
Total	$(0.2–7.4)\times10^{-3}$	$(0.6–2.8)\times10^{-2}$	$(2.6–9.7)\times10^{-2}$	$(0.5–3.7)\times10^{-2}$	$(2.6–3.3)\times10^{-2}$	$+(4.9–13.0)\times10^{-2}$ $-(9.4–36.5)\times10^{-2}$

uncertainties are p_T dependent for each source. The total absolute systematic uncertainties are the quadratic sums of the different contributions.

V. RESULTS

The measured dielectron v_2 as a function of p_T for $M_{ee} < 0.14$ GeV/c^2 in different centralities from Au + Au collisions at $\sqrt{s_{NN}} = 200$ GeV are shown in Fig. 19. For comparison, the charged and neutral pion v_2 results [42,51] are also shown in Fig. 19. We parametrize the pion v_2 from low to high p_T, perform the Dalitz decay simulation, and obtain the expected dielectron v_2 from π^0 Dalitz decay shown by the dashed curve. The ratio of the measured dielectron v_2 to the expected is presented in Fig. 20. The simulated dielectron v_2 from π^0 Dalitz decay is consistent with our measurements in all centralities within 5–10%. We note that different nonflow effects in the dielectron v_2 analysis and the PHENIX π v_2 analysis might contribute to differences between data and simulation.

Figure 21 shows the dielectron v_2 as a function of p_T in minimum-bias Au + Au collisions at $\sqrt{s_{NN}} = 200$ GeV in six different mass regions: π^0, η, charm + ρ^0, ω, ϕ, and charm+thermal radiation, as defined in Table III. We find that the expected dielectron v_2 (dashed curve) from π^0, η, ω, and ϕ decays is consistent with the measured dielectron v_2 for $M_{ee} < 1.1$ GeV/c^2. The dielectron v_2 in the ϕ mass region is consistent with the ϕ meson v_2 measured through the decay channel $\phi \to K^+K^-$ [44]. In addition, in the charm+thermal radiation mass region, dielectron v_2 can be described by a $c\bar{c}$ contribution within experimental uncertainties.

With the measured p_T-differential v_2 presented above and cocktail spectrum shapes detailed in Sec. III D, we obtain the dielectron integral v_2 for $|y_{e^+e^-}| < 1$, which is the yield weighted average for $p_T(e^+e^-) > 0$. For the low p_T region where the analysis is not applicable, we use the simulated differential v_2 for the extrapolation. The p_T spectra of dielectrons might be different from those of cocktail components. For the mass region $0.2 < M_{ee} < 1.0$ GeV/c^2, we also use dielectron

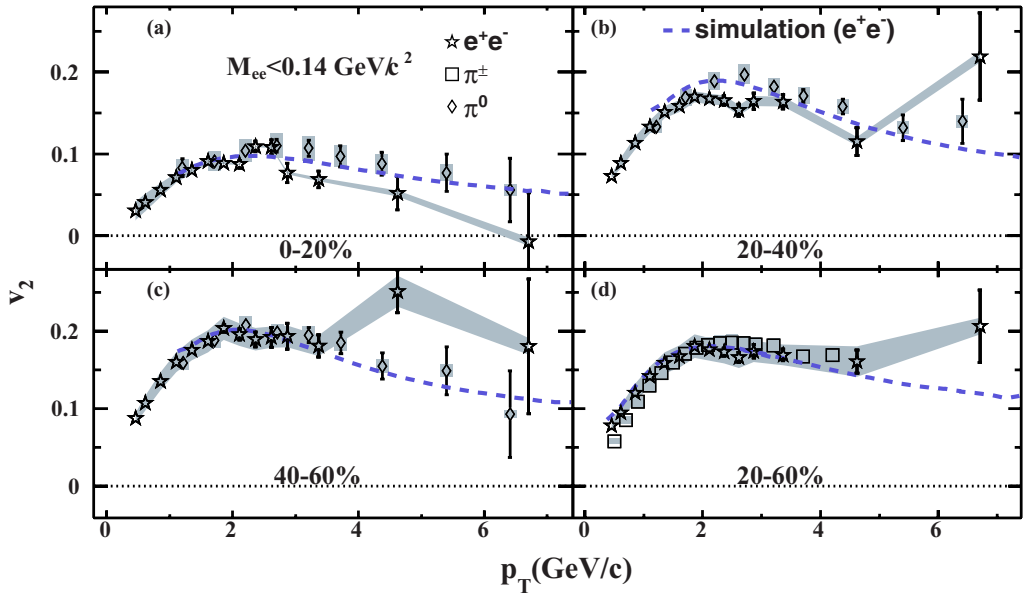

FIG. 19. (Color online) The dielectron v_2 in the π^0 Dalitz decay region (star symbol) as a function of p_T in different centralities from Au + Au collisions at $\sqrt{s_{NN}} = 200$ GeV. Also shown are the charged (square) [51] and neutral (diamond) [42] pion v_2, and the expected dielectron v_2 (dashed curve) from π^0 Dalitz decay. The bars and bands represent statistical and systematic uncertainties, respectively.

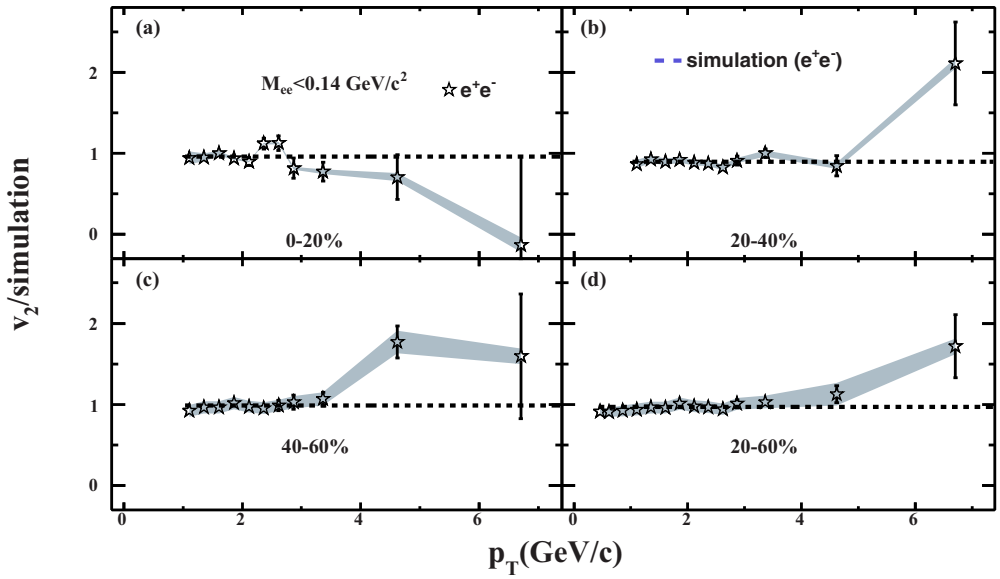

FIG. 20. (Color online) The ratio of the measured dielectron v_2 in the π^0 Dalitz decay region over the expected dielectron v_2 from π^0 Dalitz decay as a function of p_T in different centralities from Au + Au collisions at $\sqrt{s_{NN}} = 200$ GeV. The dashed line is a constant fit to the ratio. The bars and bands represent statistical and systematic uncertainties, respectively.

p_T spectra measured by PHENIX [10] and obtain the integral v_2 in these mass regions. The difference between this and the default case contributes additional systematic uncertainties for the integral v_2 measurements, which are smaller than those from other sources detailed in Sec. IV. Figure 22 shows the dielectron integral v_2 from data and simulation for $|y_{e^+e^-}| < 1$

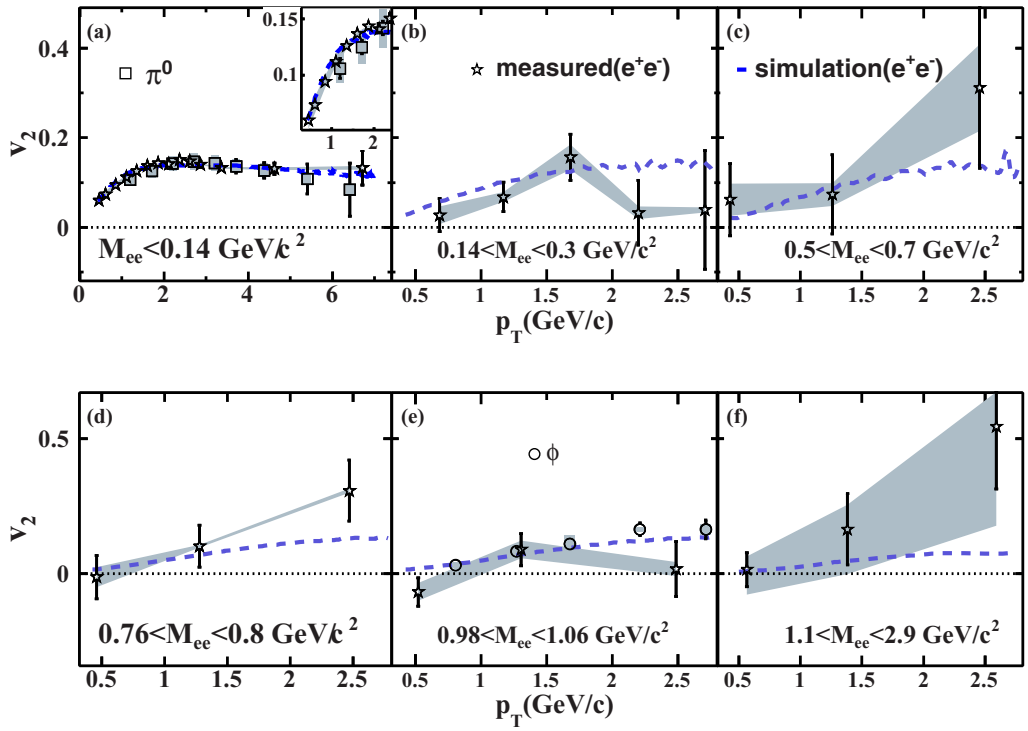

FIG. 21. (Color online) (a)–(f) The dielectron v_2 as a function of p_T in minimum-bias Au + Au collisions at $\sqrt{s_{NN}} = 200$ GeV for six different mass regions: π^0, η, charm + ρ^0, ω, ϕ, and charm + thermal radiation. Also shown are the neutral pion [42] v_2 and the ϕ meson v_2 [44] measured through the decay channel $\phi \to K^+K^-$. The expected dielectron v_2 (dashed curves) from π^0, η, ω, and ϕ decays in the relevant mass regions are shown in panels (a)–(e) while that from $c\bar{c}$ contributions is shown in panel (f). The bars and bands represent statistical and systematic uncertainties, respectively. The full difference between mixed-event unlike-sign and same-event like-sign background subtraction contributes to the lower bound of the systematic uncertainties, which leads to asymmetric systematic uncertainties in panel (f).

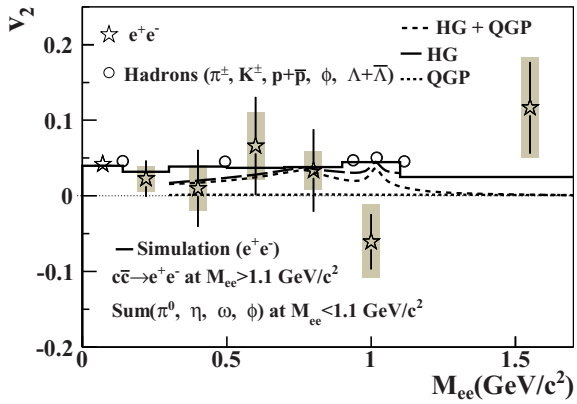

FIG. 22. (Color online) The p_T-integrated dielectron v_2 as a function of M_{ee} in minimum-bias Au + Au collisions at $\sqrt{s_{NN}} = 200$ GeV. Also shown are the corresponding dielectron v_2 simulated from π^0, η, ω, and ϕ decays and a $c\bar{c}$ contribution. The theoretical calculations from hadronic matter and QGP thermal radiation and the sum of these two sources [54] are shown for comparisons. The v_2 for hadrons π, K, p, ϕ, and Λ are also shown for comparison. The bars and boxes represent statistical and systematic uncertainties, respectively. The systematic uncertainty for the first data point is smaller than the size of the marker.

for minimum-bias Au + Au collisions at $\sqrt{s_{NN}} = 200$ GeV. Also shown are the corresponding dielectron v_2 simulated from π^0, η, ω, and ϕ decays and the $c\bar{c}$ contribution.

For $M_{ee} < 1.1$ GeV/c^2, the v_2 from simulated π^0, η, ω, and ϕ decays is consistent with the measured dielectron v_2 within experimental uncertainties. For the measured range $1.1 < M_{ee} < 2.9$ GeV/c^2, the estimated v_2 magnitude from the simulated $c\bar{c}$ contribution is consistent with the measurement.

We also observe the measured dielectron integral v_2 as a function of M_{ee} to be comparable to the hadron v_2 at a given hadron mass. The hadron v_2 integral is obtained from the measured p_T differential v_2 [44,52,53] and spectrum shapes [41]. Also shown in Fig. 22 is a comparison to theoretical calculations for the v_2 of thermally radiated dileptons from a hadron gas (HG) and the QGP separately, and for the sum of the two with a calculation of the relative contributions from HG and QGP [54]. In this calculation, the dilepton v_2 are studied with 3+1-dimensional viscous hydrodynamics. The QGP contribution comes from leading order quark-antiquark annihilation, while for the HG emission rate the vector dominance model is used. According to this calculation, the dilepton radiation is QGP dominated for $M_{ee} > 1.3$ GeV/c^2. However, the charm v_2 must first be subtracted in order to compare directly with the theoretical calculation. In the future, with more data and more precise measurements of the charm contribution to the dielectron spectrum and v_2, hadron cocktail contributions may be subtracted from the measurements and the v_2 of excess dielectrons may be obtained. The excess dielectron spectrum and v_2 measurements as a function of p_T in the mass region $1.3 < M_{ee} < 2.9$ GeV/c^2 will enable a direct comparison to theoretical results for QGP thermal radiation [54].

VI. SUMMARY

In summary, we report the first dielectron azimuthal anisotropy measurement from Au + Au collisions at $\sqrt{s_{NN}} = 200$ GeV. The dielectron v_2 for $M_{ee} < 1.1$ GeV/c^2 as a function of p_T is found to be consistent with the v_2 for π^0, η, ω, and ϕ decays. For $1.1 < M_{ee} < 2.9$ GeV/c^2, the measured dielectron v_2 is described by the $c\bar{c}$ contribution within statistical and systematic uncertainties. With more data taken in the future, STAR will be in a good position to distinguish a QGP-dominated scenario from a HG-dominated one.

ACKNOWLEDGMENTS

We thank C. Gale, R. Rapp, G. Vujanovic, and C. Young for valuable discussions and for providing the theoretical calculations. We thank the RHIC Operations Group and RCF at BNL, the NERSC Center at LBNL, the KISTI Center in Korea, and the Open Science Grid consortium for providing resources and support. This work was supported in part by the Offices of NP and HEP within the US DOE Office of Science, the US NSF, CNRS/IN2P3, FAPESP CNPq of Brazil, the Ministry of Education and Science of the Russian Federation, NNSFC, CAS, MoST, and MoE of China, the Korean Research Foundation, GA and MSMT of the Czech Republic, FIAS of Germany, DAE, DST, and CSIR of India, the National Science Centre of Poland, the National Research Foundation (NRF-2012004024), the Ministry of Science, Education and Sports of the Republic of Croatia, and RosAtom of Russia.

[1] J. Adams *et al.*, Nucl. Phys. A **757**, 102 (2005).
[2] I. Arsene *et al.*, Nucl. Phys. A **757**, 1 (2005); K. Adcox *et al.*, *ibid.* **757**, 184 (2005); B. B. Back *et al.*, *ibid.* **757**, 28 (2005).
[3] R. Rapp and J. Wambach, Adv. Nucl. Phys. **25**, 1 (2002).
[4] G. David, R. Rapp, and Z. Xu, Phys. Rep. **462**, 176 (2008).
[5] G. Agakichiev *et al.*, Eur. Phys. J. C **41**, 475 (2005).
[6] R. Arnaldi *et al.*, Phys. Rev. Lett. **96**, 162302 (2006).
[7] G.E. Brown and M. Rho, Phys. Rep. **269**, 333 (1996).
[8] R. Rapp and J. Wambach, Eur. Phys. J. A **6**, 415 (1999).
[9] K. Dusling, D. Teaney, and I. Zahed, Phys. Rev. C **75**, 024908 (2007); H. van Hees and R. Rapp, Nucl. Phys. A **806**, 339 (2008); T. Renk and J. Ruppert, Phys. Rev. C **77**, 024907 (2008).
[10] A. Adare *et al.*, Phys. Rev. C **81**, 034911 (2010).
[11] L. Adamczyk *et al.*, Phys. Rev. Lett. **113**, 022301 (2014); a longer version (unpublished).
[12] R. Rapp, J. Wambach, and H. van Hees, in *Relativistic Heavy-Ion Physics*, edited by R. Stock, Landolt Börnstein New Series I/23A (Springer, Berlin, 2010), Chap. 4-1.
[13] O. Linnyk, W. Cassing, J. Manninen, E. L. Bratkovskaya, and C. M. Ko, Phys. Rev. C **85**, 024910 (2012).
[14] H.-j. Xu, H.-f. Chen, X. Dong, Q. Wang, and Y.-f. Zhang, Phys. Rev. C **85**, 024906 (2012).
[15] A. Adare *et al.*, Phys. Rev. Lett. **104**, 132301 (2010).
[16] A. M. Poskanzer and S. A. Voloshin, Phys. Rev. C **58**, 1671 (1998).
[17] A. Adare *et al.*, Phys. Rev. Lett. **109**, 122302 (2012).

[18] H. van Hees, C. Gale, and R. Rapp, Phys. Rev. C **84**, 054906 (2011).
[19] R. Chatterjee, D. K. Srivastava, U. Heinz, and C. Gale, Phys. Rev. C **75**, 054909 (2007).
[20] A. Adare *et al.*, Phys. Lett. B **670**, 313 (2009).
[21] B. Bonner *et al.*, Nucl. Instrum. Methods A **508**, 181 (2003); M. Shao *et al.*, *ibid.* **492**, 344 (2002); J. Wu *et al.*, *ibid.* **538**, 243 (2005).
[22] J. M. Landgraf *et al.*, Nucl. Instrum. Methods A **499**, 762 (2003).
[23] K. H. Ackermann *et al.*, Nucl. Instrum. Methods A **499**, 624 (2003).
[24] M. Anderson *et al.*, Nucl. Instrum. Methods A **499**, 659 (2003).
[25] H. Bichsel, Nucl. Instrum. Methods A **562**, 154 (2006).
[26] Y. Xu *et al.*, Nucl. Instrum. Methods A **614**, 28 (2010).
[27] M. Shao *et al.*, Nucl. Instrum. Methods A **558**, 419 (2006).
[28] J. Adams *et al.*, Phys. Lett. B **616**, 8 (2005); L. Ruan, Ph.D. thesis, University of Science and Technology of China, 2005, arXiv:nucl-ex/0503018 (unpublished).
[29] W. J. Llope *et al.*, Nucl. Instrum. Methods A **522**, 252 (2004).
[30] C. Adler *et al.*, Phys. Rev. Lett. **89**, 202301 (2002).
[31] J. Adams *et al.*, Phys. Rev. Lett. **94**, 062301 (2005).
[32] L. Adamczyk *et al.*, Phys. Rev. C **86**, 024906 (2012).
[33] J. Zhao, Ph.D. thesis, Shanghai Institute of Applied Physics, 2013, https://drupal.star.bnl.gov/STAR/theses/phd-32 (unpublished).
[34] S. A. Voloshin, A. M. Poskanzer, and R. Snellings, in *Relativistic Heavy Ion Physics*, Landolt-Börnstein Vol. 1/23 (Springer-Verlag, Berlin, 2010), pp. 5–54.
[35] L. Adamczyk *et al.*, Phys. Rev. C **88**, 014902 (2013).
[36] B. I. Abelev *et al.*, Phys. Rev. C **77**, 054901 (2008).
[37] B. I. Abelev *et al.*, Phys. Rev. Lett. **97**, 152301 (2006).
[38] B. I. Abelev *et al.*, Phys. Rev. C **79**, 034909 (2009).
[39] B. I. Abelev *et al.*, Phys. Rev. C **79**, 064903 (2009); J. Adams *et al.*, Phys. Lett. B **612**, 181 (2005).
[40] S. S. Adler *et al.*, Phys. Rev. C **75**, 024909 (2007).
[41] Z. Tang, Y. Xu, L. Ruan, G. van Buren, F. Wang, and Z. Xu, Phys. Rev. C **79**, 051901(R) (2009); M. Shao, L. Yi, Z. Tang, H. Chen, C. Li, and Z. Xu, J. Phys. G **37**, 085104 (2010).
[42] S. Afanasiev *et al.*, Phys. Rev. C **80**, 054907 (2009).
[43] J. Adams *et al.*, Phys. Rev. C **72**, 014904 (2005).
[44] B.I. Abelev *et al.*, Phys. Rev. Lett. **99**, 112301 (2007).
[45] N. M. Kroll and W. Wada, Phys. Rev. **98**, 1355 (1955).
[46] L. Ruan *et al.*, Nucl. Phys. A **855**, 269 (2011); B. Huang, Ph.D. thesis, University of Science and Technology of China, 2011 (unpublished).
[47] T. Sjöstrand *et al.*, Comput. Phys. Commun. **135**, 238 (2001).
[48] L. Adamczyk *et al.*, Phys. Rev. D **86**, 072013 (2012).
[49] H. Agakishiev *et al.*, Phys. Rev. D **83**, 052006 (2011).
[50] A. Adare *et al.*, Phys. Rev. C **84**, 044905 (2011).
[51] A. Adare *et al.*, Phys. Rev. C **85**, 064914 (2012).
[52] A. Adare *et al.*, Phys. Rev. Lett. **98**, 162301 (2007).
[53] J. Adams *et al.*, Phys. Rev. Lett. **92**, 052302 (2004).
[54] G. Vujanovic, C. Young, B. Schenke, S. Jeon, R. Rapp, and C. Gale, Nucl. Phys. A **904-905**, 557c (2013); Phys. Rev. C **89**, 034904 (2014).